Emission dynamics of optically driven aluminum nitride quantum emitters

Yanzhao Guo, John P. Hadden, Rachel N. Clark, Samuel G. Bishop, and Anthony J. Bennett*
Translational Research Hub, Cardiff University, Maindy Road, Cardiff, CF24 4HQ, United Kingdom
and School of Engineering, Cardiff University, Queen's Buildings, The Parade, Cardiff, CF24 3AA, United Kingdom

(Received 9 October 2023; revised 26 April 2024; accepted 28 June 2024; published 22 July 2024)

Aluminum nitride is a technologically important wide band-gap semiconductor which has been shown to host bright quantum emitters. We use photon emission correlation spectroscopy (PECS), time-resolved photoluminescence (TRPL), and state-population dynamic simulations to probe the dynamics of emission under continuous wave (CW) and pulsed optical excitation. We infer that there are at least four dark shelving states, which govern the TRPL, bunching, and saturation of the optical transition. We study in detail the emission dynamics of two quantum emitters (QEs) with differing power-dependent shelving processes, hypothesized to result from charge ionization and recombination. These results demonstrate that photon bunching caused by shelving the system in a dark state inherently limits the saturation rate of the photon source. In emitters where increasing optical power deshelves the dark states, we observe an increased photon emission intensity.

DOI: 10.1103/PhysRevB.110.014109

I. INTRODUCTION

Single quantum emitters (QEs) in wide band-gap semiconductors are promising single-photon sources which can operate up to room temperature [1–3]. In addition to the numerous luminescent defects in diamond [4], there are more recent reports of quantum light emission in silicon carbide [5], silicon nitride [6], and the group III-nitrides. Many of the QEs reported in the later category display favorable optical properties including a high Debye-Waller factor of 0.39 in gallium nitride (GaN) [7], a high continuous wave (CW) photon detection rate of 3.7 MHz from a single emitter in hexagonal boron nitride (hBN) [8], and availability of low-cost epitaxial wafers of AlGaN [9]: therefore, each potentially offers advantages for scalable quantum nanophotonics [10]. Moreover, some QEs in hBN and GaN were reported with optically detected magnetic resonance (ODMR) response [11–13], which makes them attractive for quantum sensing.

Another member of the III-nitride semiconductor family, aluminum nitride (AlN) is a commercially important semiconductor for high-power and optoelectronic devices. The discovery of QEs hosted in a material with advanced crystal growth technology and established industrial fabrication processes paves the way to wafer-scale device manufacture at low marginal cost. Various QEs have been reported within its ultrawide ~ 6.015 eV band gap. For example, Lu *et al.* found QEs with 580–650 emission and low multiphoton emission probability [$g^{(2)}(0) < 0.1$] by He implantation into a commercial AlN film on a sapphire substrate [14]. Our previous work also reported similar emitters in an as-grown AlN film [15], and recently enhanced their detected photoluminescence (PL) saturation rate to almost 1 MHz using an index-matched solid immersion lens [7]. Wang *et al.* fabricated emitters with near 0.65 Debye-Waller factor emitting near 600 nm in free-standing AlN by laser writing [16].

Despite this interest in AlN's QEs, their physical origin and electronic structure remain uncertain. Theoretical calculations have shown that AlN QEs may host solid-state qubits with long qubit-state lifetime due to their small spin-orbit splitting [17], but it is not certain that the observed QEs are the same as those simulated. Previous studies on AlN QEs reported photon bunching associated with transition to one longer-lived metastable dark "shelving state" [7,14,16,18]. This shelving process occurs when the population of the excited state relaxes to a metastable state without a photon being detected, either through a nonradiative process or photon emission at a wavelength outside the detection range. However, as we show, a single shelving state is insufficient to explain their full PL behavior. Better understanding of their radiative and nonradiative transitions may allow optimization of quantum emission, for example, through state preparation, or by identifying features that allow preselection of emitters with a certain performance. The existence of a dark shelving state is a prerequisite for the fluorescence depletion mechanism which can be used for stimulated depletion spectroscopy [19,20], and superresolution microscopy applications [19,21]. More fundamentally, determining the electronic structure of these QEs is also an important step in the effort to determine their physical origin.

In this paper, we use optical excitation to probe the emission dynamics in two emitters with differing power-dependent behaviors. Photon emission correlation spectroscopy (PECS) and time-resolved photoluminescence (TRPL) are compared to simulations showing that there are at least six internal

*Contact author: BennettA19@cardiff.ac.uk

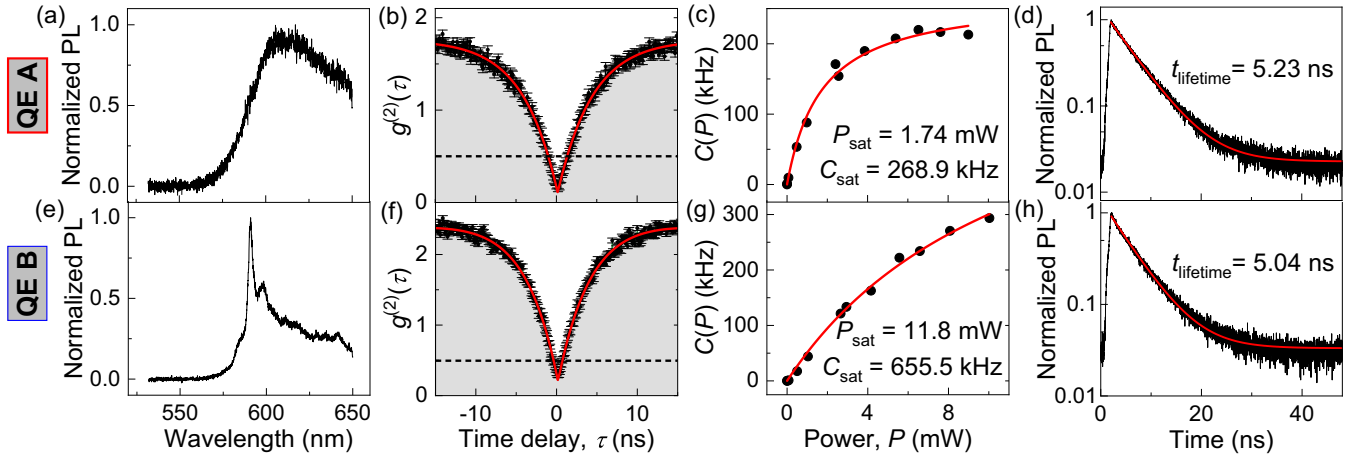

FIG. 1. Characterization of two quantum emitters in AlN at room temperature: QE A (first row) and QE B (second row). (a) and (e) show the spectra between 532 and 650 nm. (b) and (f) are the photon emission correlation histograms, normalized, without background correction (black points), and fit using an empirical model discussed in the text (red line). Error bars represent Poissonian uncertainties based on the photon counts in each bin. (c) and (g) are the CW-PL saturation behaviors (black points) as a function of laser power, fit using Eq. (1). (d) and (h) show the excited-state lifetime measurement, fit with a single exponential (red line).

energy levels in each emitter (one ground state, one radiative excited state, and four shelving states). The two emitters have different laser power-dependent shelving and deshelving processes. These results demonstrate that photon bunching caused by shelving the system in dark states inherently limits the saturation rate of the photon source. However, in the emitters we identify that can be optically driven out of the dark state, bunching is suppressed at high power, and we observe an increased photon emission intensity.

II. RESULTS AND DISCUSSION

We use a home-built confocal microscope to study isolated single QEs in a commercial single-crystal c-plane 1 μm AlN film on a sapphire template at ambient conditions [15] with an emitter density of 0.09 μm^{-2}. By investigating ten QEs in this AlN film we identify QEs in which shelving processes are found to increase or decrease with laser power, exemplified by emitters QE A and QE B, respectively, which are studied in detail. All the measurements are made with the laser polarization aligned to the QE's preferred absorption polarization angle [15] with no polarizer in the collection path. Typical absorption and emission polarization characterization is available in the Supplemental Material (SM) [22]. The collection optical filter window is between 532 and 650 nm covering their dominant spectral emission range. Further details on the system are given in Appendix A 1. These emitters often show spectral and intensity fluctuations on the milliseconds-to-seconds timescale at room temperature [15], but display consistent spectral and photodynamic properties after months of measurements in ambient conditions.

In Fig. 1(a), the spectrum of QE A consists of a single broad feature we attribute to the phonon sideband (PSB) extending from 600 nm to beyond the optical filtering cutoff at 650 nm. The absence of a resolvable zero phonon line (ZPL) suggests a low Debye-Waller factor, consistent with some previous reports [7,15]. In contrast, in Fig. 1(e) QE B displays a strong ZPL at 590 nm with a PSB more comparable to the $N_{Al}O_N$ type defect proposed a recent study [16]. The correlation histograms of both QEs display substantial bunching over hundreds of nanoseconds associated with the later discussion of shelving behavior, nevertheless, the values of $g^{(2)}(0)$ for QE A and QE B are 0.16 ± 0.04 and 0.29 ± 0.03, respectively, in Figs. 1(b) and 1(f). Such low $g^{(2)}(0)$ suggests a single transition is involved in photon emission across this spectral feature. Another signature of a quantized emitter is its photoluminescence (PL) intensity saturation with CW excitation. Figures 1(c) and 1(g) show this data fitted with

$$C(P) = \frac{C_{sat} P}{P + P_{sat}}, \tag{1}$$

where $C(P)$ is the steady-state PL rate as a function of power P, C_{sat} is the saturation PL rate, and P_{sat} is the corresponding saturation power. QE B requires 6.8 times higher P_{sat} and has 2.4 times higher C_{sat}. The phonon-sideband is truncated via a 650 nm short pass filter which suppresses the emission from the sapphire substrate. Thus, were we able to detect that the full spectrum in the saturated intensities would be higher. Despite the difference in saturation behavior, the two QEs both have a $\sim$ 5 ns radiative lifetime obtained by fitting a single exponential decay function to the TRPL data in Figs. 1(d) and 1(h), suggesting the difference in saturation intensity is a result of differing non-radiative pathways [20,21].

To further explore the dynamics of photon emission in these QEs, PECS was recorded for QE A and QE B [Figs. 2(a) and 2(b)] over 100 μs timescale. The minimum time bin in the PECS is 100 ps. Least-squares fits to the $g^{(2)}(\tau)$ data are shown using the empirical equation [23–26]

$$g^{(2)}(\tau) = 1 - C_1 e^{-|\tau|\cdot r_1} + \sum_{i=2}^{N} C_i e^{-|\tau|\cdot r_i}, \tag{2}$$

with varying numbers of variables in the sum, denoted i. As we shall show later, the total number of levels in the sum indicates the number of shelving states in the QE, N-1. Here, r_1 is the antibunching rate, C_1 is the antibunching amplitude,

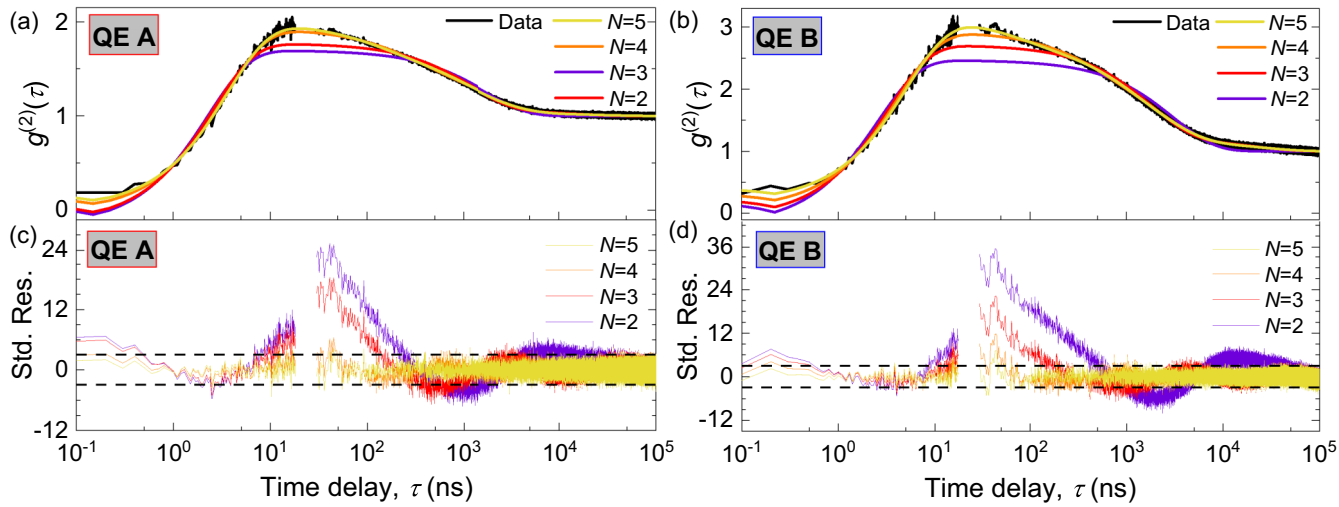

FIG. 2. Photon emission correlation spectroscopy (PECS). Black lines in (a) and (b) are the PECS of QE A and QE B, fit using empirical equation (2) for $N = 2$, 3, 4, and 5. (c) and (d) are the corresponding residuals from the fits to QE A and QE B, respectively. The raw data between 22–35 ns is masked to hide reflections from the APDs' backflash.

r_i for $i \geqslant 2$ are bunching rates, and C_i for $i \geqslant 2$ are the corresponding bunching amplitudes. Then the number of resolvable timescales N is determined by calculating and comparing the reduced chi-squared statistic, r-square for each best-fit model. Figures 2(c) and 2(d) show standardized residuals for each QE for the best-fit empirical model at different N. Interestingly, for both QEs an adequate fit (within the noise level of the data) is provided by the $N = 5$ model, suggesting at least four shelving levels, plus the radiative state, are present. In addition, their timescales range from ns to tens of μs which are much more complex than the simple one shelving process with sub-μs timescale in the previous reports in AlN [15]. However, this behavior is comparable to some optically addressable QEs in hBN [12,27]. These shelving states could arise from different spin manifolds or charge states internal to the QE or fluorescence intermittency caused by charging of nearby trap sites [26,28,29]. It is possible to directly probe differences in the shelving dynamics under optical driving, and when the QEs are not illuminated, using time gating. In Figs. 3(a) and 3(b), we excited QE A and QE B with pairs of square 2 μs laser pulses with variable spacing, τ_{double}. The first pulse pumps the population into the shelving states, resulting in an exponentially decreasing intensity until a steady state is reached. Dependent on the delay between the two pulses τ_{double} we observe a revival of the PL emission intensity at the start of the second pulse, as the population decays back to the ground state in Figs. 3(a) and 3(b) [30]. Integrating the first 120 ns PL at the start of the second pulse, we plot the PL revival curve in Figs. 3(c) and 3(d). The double exponential gives an adequate fit, indicating more than one decay rate associated with the shelving states. This result further supports the inference from Fig. 2 that multiple shelving states exist. The fact that Figs. 3(c) and 3(d) can be modeled with two shelving states when there is no optical power during τ_{double}, rather than the four shelving states required for $g^{(2)}(\tau)$, may be a result of some laser-driven deshelving mechanism in QE A and QE B.

To investigate the power dependence of shelving, the power-dependent $g^{(2)}(\tau)$ under CW excitation is fitted with Eq. (2) for $N = 5$. In Figs. 4(a) and 4(b), QE A and QE B show nearly opposite power-dependent bunching mechanisms, indicating the different power-dependent shelving dynamics. Figures 4(c) and 4(d) summarize the fitting results of the antibunching and bunching rates and amplitudes for QE A and QE B, respectively.

For QE A, the dominant $C_{2,3}$ bunching amplitudes rise with laser power, thus the bunching increases in Fig. 4(a). This trend reveals that the increasing laser power transfers the population from the excited state to the shelving states, reducing the PL intensity [20]. This power-enhanced bunching behavior is consistent with previous reports on these same samples [7,15]. In contrast, for QE B, the bunching amplitudes $C_{2,4,5}$ fall with power, resulting in a net reduction in bunching with increasing laser intensity. In other words, increasing laser power transfers the population out of the shelving states. This enables QE B to be an efficient radiative emitter at high laser power [20,21,31].

Furthermore, the antibunching rates for QE A and QE B scale linearly with power, indicating a single radiative state [18,25]. For QE A, bunching rate r_3 shows linear scaling and zero offset with laser power, which suggests the transition between the radiative state and the shelving states is laser driven. Moreover, r_2 and r_4 for QE A have a nonzero value at low power due to spontaneous emission and yet linearly increase with power, suggesting both optical pumping and spontaneous decay exist [25]. Regarding QE B, the bunching rates are more complicated which are zero at low power (no decay by spontaneous emission from excitation state) but saturate at high power, suggesting the transitions can be optically driven between shelving states [20,25,32].

The power-dependent optical dynamics can also be probed with TRPL under 2 μs square pulsed excitation in Figs. 5(a) and 5(b). These saturation behaviors also reveal that the population of the excited state in QE A is rapidly shelved at

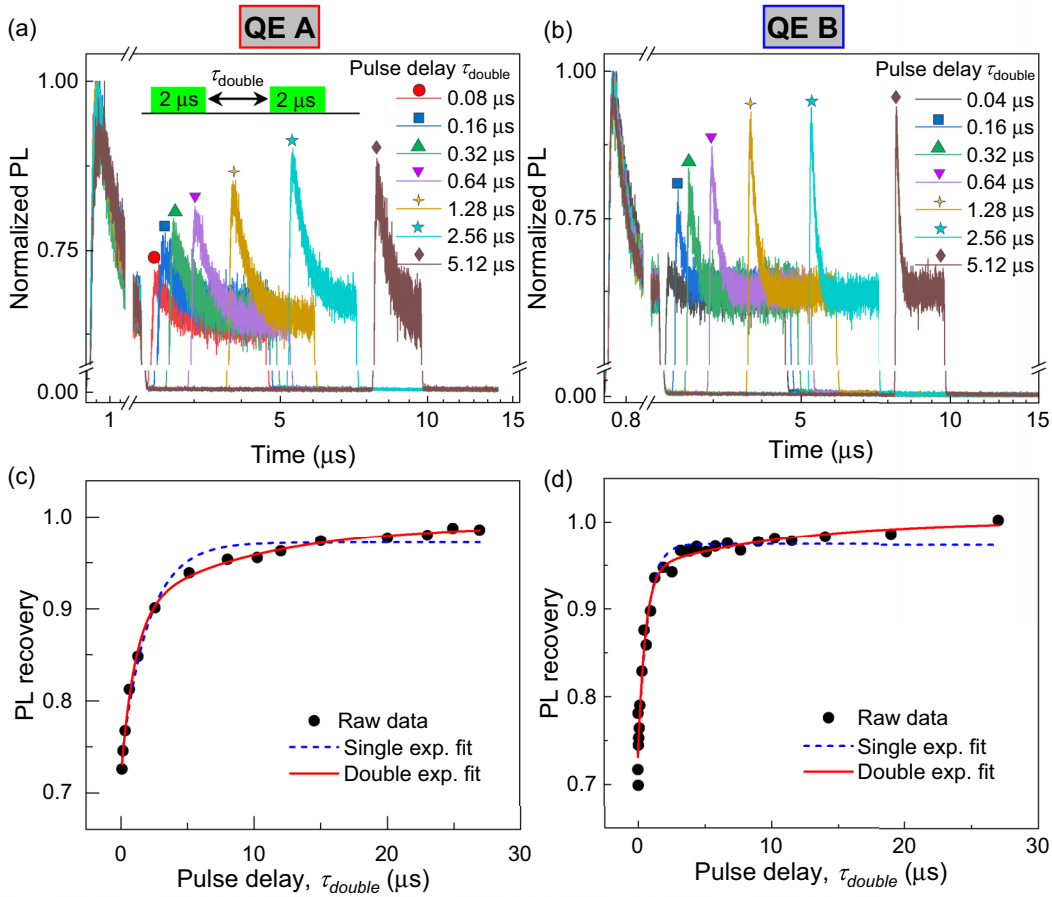

FIG. 3. Double pulse laser excitation. (a) and (b) are the TRPL of QE A and QE B under double pulse laser excitation. The inset in (a) is the train of the laser pulses. (c) and (d) represent the PL revival behavior under the second pulse excitation in (a) and (b) fitted by single exponential and double exponential equations.

high power leading to reduced steady-state radiative emission. QE B requires an 18.2 times higher laser power to saturate than QE A. In contrast, QE B remains an effective emitter at high power. The discrepancy between this value and the ratio obtained from CW saturation [Figs. 1(c) and 1(g)] may be a result of using short 2 µs pulses, which does not allow enough time for the longer timescale decay processes to reach equilibrium. We fit the TRPL with a single exponential decay function to extract a decay rate and normalized steady-state PL rate in Figs. 5(c) to 5(f). The shelving rate of QE A is superlinear and that of QE B is sublinear. Referring to the example of the negatively charged nitrogen-vacancy NV^- center in diamond and QEs in hBN, these saturation behaviors may stem from optically pumped shelving (e.g., charge ionization and conversion) [20,25,32].

To qualitatively understand these power-dependent behaviours, we use a state population dynamics simulation [24] in Fig. 6 with two different shelving models. For simplicity, we perform this simulation with only three energy levels and vary only the power dependence of the transitions. This approach enables us to understand the trends in the power dependence of PECS and TRPL without the complexity of solving for all $N = 5$ energy levels. Information regarding these simulations is given in Appendix A 2. Each model consists of a ground state (GS) 1, an excited state (ES) 2, and a shelving state (SS) 3, where transitions between the states are labeled k_{ij}, where i and j are the initial and final state numbers in insert of Fig. 6(a). The transition rates of the two models are shown in Table I, but briefly, in model I, we assume both shelving and deshelving transitions are driven by the laser, whereas in model II there is a fixed fast shelving rate and optically pumped deshelving rate. Figures. 6(c)–6(e) show the results fitting these two models to PECS measurements with Eq. (2) for $N = 2$. The steady-state PL saturation is also simulated in Fig. 6(f). We note that there are other possible models containing a single shelving level with power-dependent rates (see SM [22]) and that these models could be extended to include all four shelving states inferred from Fig. 2, however, the two models I and II considered here are sufficient to provide qualitative agreement with our

TABLE I. Simulation rate table.

Model	Shelving rate	De-shelving	Emission transition rate
I	$k_{23} = 0.05{*}k_{12}$[a]	$k_{31} = 0.03{*}k_{12}$[a]	$k_{21} = 200$ MHz
II	$k_{23} = 10$ MHz	$k_{31} = 0.03{*}k_{12}$[a]	$k_{21} = 200$ MHz

[a]Optically excited rate $k_{12} = \alpha_{12}{*}k_{21}$, α_{12}=0.01, 0.05, 0.1, 0.2, 0.5, 1, 2, 5, 10.

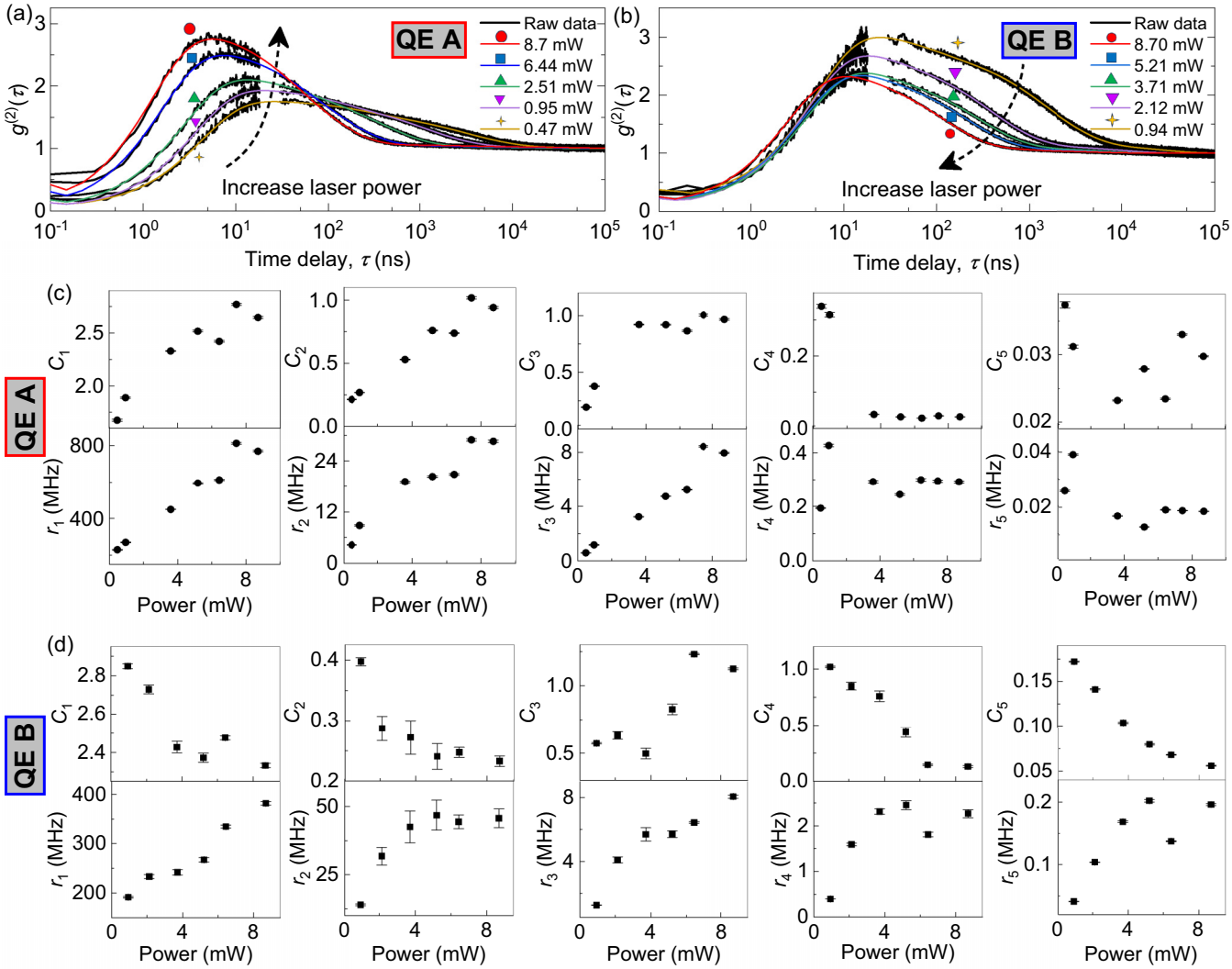

FIG. 4. Power-dependent PECS from (a) QE A and (b) QE B. Each autocorrelation is fitted with Eq. (2) and $N = 5$. (c) and (d) are amplitudes C_i and rates r_i arising from fitting Eq. (2) for QE A and QE B, respectively.

experimental results. In Fig. 6(c) the antibunching rates (r_1) of these two models are linearly rising with pump power, offset by the spontaneous emission rate, which is consistent with the results of QE A and QE B. Moreover, model I and model II display opposite power-dependent bunching dynamics. Specifically, model I shows an increasing bunching amplitude comparable to what is observed in QE A. On the other hand, model II shows a reduced bunching amplitude comparable to what is seen in QE B.

Interestingly, the TRPL shelving rates of model I and model II in Fig. 6(e) can be fitted by superlinear and sublinear functions with zero offsets, which is perfectly consistent with the TRPL results of QE A and QE B in Figs. 5(e) and 5(f). Additionally, model II shows several times higher saturation power and saturation intensity than model I in Fig. 6(f), which is comparable to the results of QE A and QE B in Figs. 1(c) and 1(g). Thus, comparing our simulation and experimental results, we conclude that QE A displays model I shelving and QE B displays model II behavior.

As the physical structure of the studied emitters is unknown it is difficult to unambiguously determine the physical origin of the shelving and deshelving behaviors we observe. However, it is instructive to compare their behavior to other well-studied emitters in other materials. We note that the behavior of QE A with shelving model I is comparable to the NV^- in diamond which displays laser-induced shelving and deshelving to the neutral nitrogen-vacancy (NV^0) charge state at high excitation power, as well as spontaneous shelving and de-shelving to the NV^- singlet states [20,33]. In contrast, at low-power QE B is fast-decaying to the shelving state resulting in a strong bunching in the PECS, while at higher laser excitation this bunching is suppressed, allowing higher emission rates by laser-induced deshelving. This is not common for single QEs under monochromatic laser excitation, but is observed in multiple laser excitation of emitters in hBN as well as the NV^- center [19–21,31]. One laser is selected to efficiently pump the ground state, while another laser repumps the population out of the shelving state, allowing recovery of the emission [19,21,31].

Based on the discussions above, a key factor for the achievable saturation PL rate of QEs is the shelving dynamics at high power. The ideal QE should have reduced shelving at high

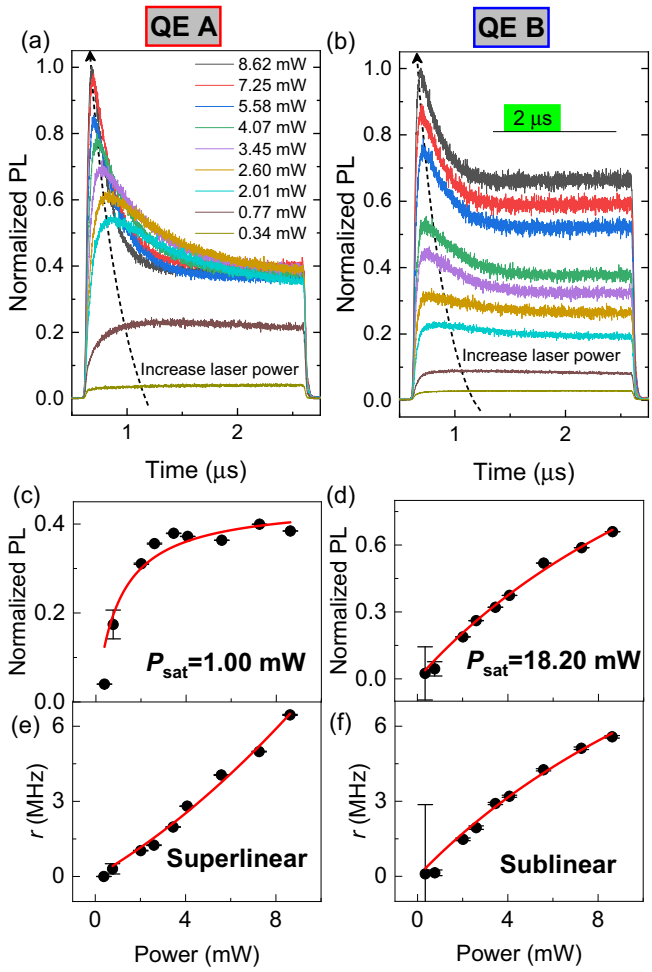

FIG. 5. Power-dependent TRPL with square excitation pulses. (a) QE A, (b) QE B, with insert showing the pulse sequence. (c) and (d) are the normalized PL saturation behaviours of the steady states. (e) and (f) are the TRPL decay rates observed in (a) and (b).

power, as observed in QE B. A second color laser could be used to efficiently repump the population from the shelving state back to the bright transition. In the best case, the nonradiative transition could be completely neglected, leading to an emitter with an intensity determined only by the spontaneous decay rate. For example, QE A would become ∼2.5 times brighter at saturation, giving >0.67 MHz PL rate, and QE B would become 1.5 times brighter leading to ∼1.0 MHz PL rate.

III. CONCLUSION

In conclusion, AlN QEs display complex optical dynamics which indicates they have internal electronic level structures with multiple charge or shelving states. We identify two different optical-power-dependent shelving behaviors associated with the charge ionization and recombination processes. We propose models of the dynamic behavior which complements previous reports and explains the quantitative features of our observations which provide an important experimental reference for future theoretical work. Future experiments could focus on the energy-dependent behavior of the shelving and deshelving processes using tunable lasers. Nevertheless, the techniques used in this paper offer a way to study the internal energy levels in the QEs of other materials. Moreover, this study will help us to design a suitable protocol to minimise the time each QE spends in metastable shelving states, resulting in an overall increased intensity.

Data supporting the findings of this study are available in the Cardiff University Research Portal at [34].

ACKNOWLEDGMENTS

The authors acknowledge the financial support provided by EPSRC via Grants No. EP/T017813/1 and No. EP/X03982X/1 and the European Union's H2020 Marie Curie ITN project LasIonDef (Grant Agreement No. 956387). RC was supported by Grant No. EP/S024441/1, Cardiff University, and the National Physical Laboratory. Sample processing was carried out in the cleanroom of the ERDF-funded Institute for Compound Semiconductors (ICS) at Cardiff University.

The corresponding author identified the following author contributions, using the CRediT Contributor Roles Taxonomy standard: Y.Z.G.: Conceptualization, methodology, software, investigation, data-curation, writing-original draft. J.P.H.: software, methodology, writing- review and editing, supervision, funding acquisition. R.C.: software, methodology, writing- review and editing, S.B.: software, methodology, writing- review and editing, A.J.B.: conceptualisation, methodology, writing- review and editing, supervision, project administration, funding acquisition.

APPENDIX: EXPERIMENTAL METHODS

1. Experiment

The sample was excited by a CW 532 nm laser (Crystal Laser) modulated by an acoustic-optic modulator (AOM) (ISOMET 553F-2) with <10 ns rise and fall time for static PL characterization, PECS and TRPL experiment. A 100 ps pulsed 520 nm laser (Picoquant P-C-520M) was used for the radiative lifetime measurement in Figs. 1(d) and 1(h). The polarization of both lasers was set by a linear polarizer and half-waveplate. Excitation and collection of photons from the sample were performed by a single objective with NA = 0.9. Collected PL was filtered by a dichroic mirror, 532 nm long-pass filter, and 650 nm short-pass filter, before detection on SPCM-AQRH silicon avalanche photodiodes (Excelitas) or a spectrometer with a silicon CCD.

TRPL was recorded with an ID900 time controller. For the lifetime measurements [Figs. 1(d) and 1(h)], the ID900 time controller records the PL histogram with a resolution of 13 ps at 20 MHz repetition frequency. For the double-pulse laser excitation and single-pulse TRPL (Fig. 4), the histogram was binned with 1 ns resolution. The spacing between each laser pulse train is 50 µs to reset the ground-state population of QEs.

PECS was recorded using the ID900 time-tagging mode, with photon arrival times acquired from two detectors in a Hanbury-Brown and Twiss interferometer. Custom software numerically correlated each photon detection on one detector

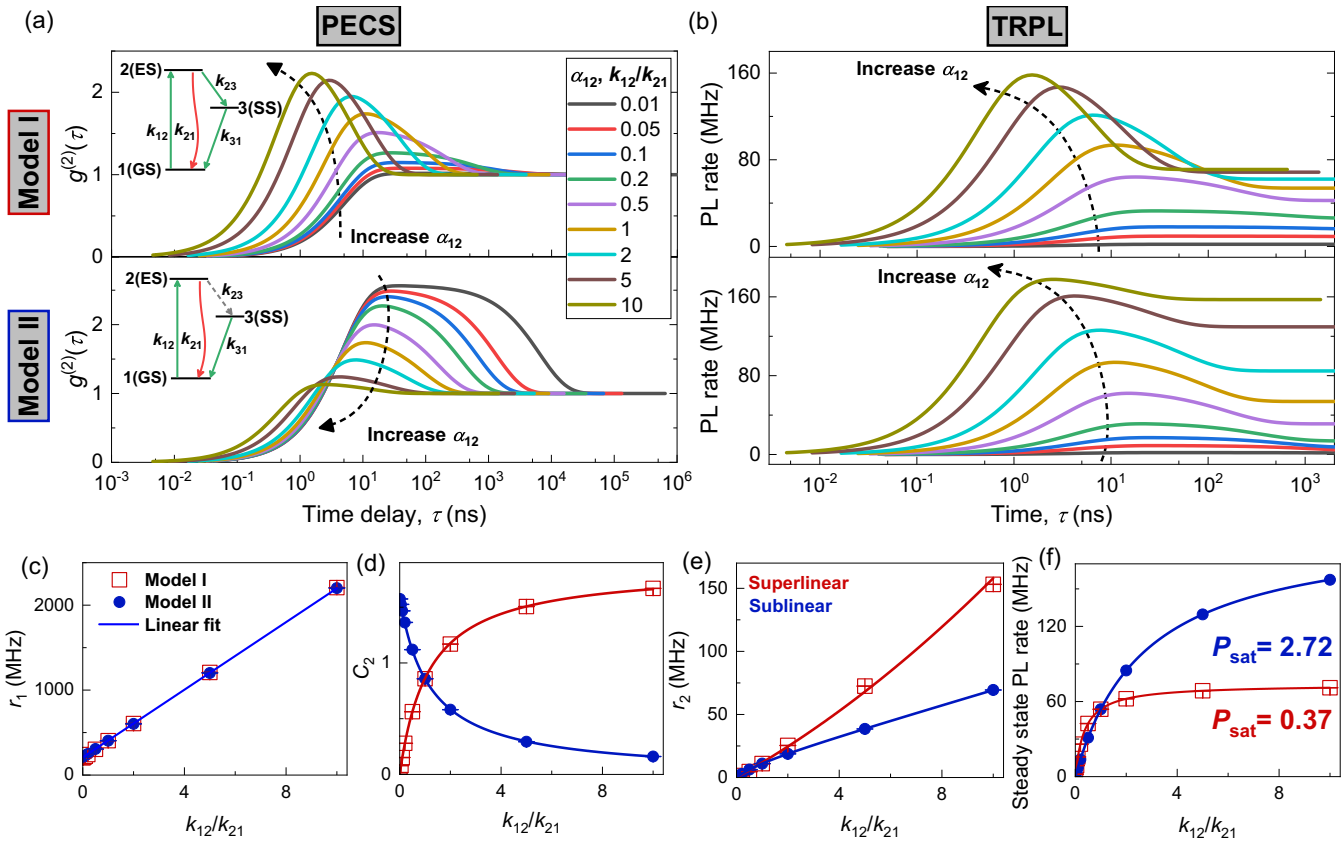

FIG. 6. State population dynamics simulation. (a) PECS and (b) TRPL simulation results for shelving model I and model II with transition rates from Table I. The inset in (a) is the proposed three-energy level shelving models I and II which include radiative emission (red arrow), optically pumped transitions (green arrows), and nonradiative transitions with a fixed spontaneous decay rate (dotted grey arrows). (c)–(e) are the best-fit parameters r_1, C_2, and r_2 determined by fitting simulated $g^{(2)}(\tau)$ data using Eq. (2) with $N = 2$. (f) is the steady-state PL saturation behavior fitted by Eq. (1). The results are plotted as a function of k_{12}/k_{21}, where $k_{21} = 200$ MHz is a fixed parameter as the spontaneous emission decay rate.

with all the other registered photons on the second detector, within a specified time window.

PECS and TRPL data are presented normalized and without background correction. The spectra and saturation data in Fig. 1 are corrected by subtraction of background emission estimated by measurements from a location 1 μm from the QE (see SM for the raw data [22]). In terms of the total system efficiency for an in-plane dipole, we consider the optical collection efficiency of the objective with NA = 0.9 (4%) [7], the fiber coupling efficiency (38%), and the detection efficiency of the single-photon detector (70%). Therefore, we estimate the total system efficiency is ∼1%. Additionally, we use a single NV^- in bulk diamond as a reference to benchmark our experiment's excitation and collection performance (see SM [22]).

2. Simulation

For any N-level electronic structure, the full optical dynamics are calculated by a system of N-coupled differential equations [24]

$$\frac{dP}{dt} = G \cdot P, \tag{A1}$$

where P is a vector of state occupation probabilities and G is the transition rate matrix, where the G_{ij} represents the transition rate from i state to j state ($i \neq j$). Each diagonal element G_{ii} corresponds to the sum of all transition rates out of state i.

Then the autocorrelation function is proportional to the population of the radiative state, $P_2(t_2)$, given the system started in ground state P_1 following the detection of a photon at t_1, and then normalizing by the steady-state population of $P_2(\infty)$ [35]. This is given by

$$g^{(2)}(\tau) = \frac{P_2[t_2|P(t_1)]}{P_2(\infty)}, \tag{A2}$$

where $\tau = t_2 - t_1$ is the time delay of $g^{(2)}(\tau)$.

[1] I. Aharonovich and M. Toth, Quantum emitters in two dimensions, Science **358**, 170 (2017).

[2] A. M. Berhane, K. Jeong, Z. Bodrog, S. Fiedler, T. Schröder, N. V. Triviño, T. Palacios, A. Gali, M. Toth, D. Englund, and

I. Aharonovich, Bright room–temperature single–photon emission from defects in gallium nitride, Adv. Mater. **29**, 1605092 (2017).

[3] M. Atatüre, D. Englund, N. Vamivakas, S.-Y. Lee, and J. Wrachtrup, Material platforms for spin-based photonic quantum technologies, Nat. Rev. Mater. **3**, 38 (2018).

[4] M. W. Doherty, N. B. Manson, P. Delaney, F. Jelezko, J. Wrachtrup, and L. C. Hollenberg, The nitrogen-vacancy colour centre in diamond, Phys. Rep. **528**, 1 (2013).

[5] S. Castelletto and A. Boretti, Silicon carbide color centers for quantum applications, J. Phys.: Photon. **2**, 022001 (2020).

[6] A. Senichev, Z. O. Martin, S. Peana, D. Sychev, X. Xu, A. S. Lagutchev, A. Boltasseva, and V. M. Shalaev, Room-temperature single-photon emitters in silicon nitride, Sci. Adv. **7**, eabj0627 (2021).

[7] S. G. Bishop, J. K. Cannon, H. B. Yağcı, R. N. Clark, J. P. Hadden, W. Langbein, and A. J. Bennett, Evanescent-field assisted photon collection from quantum emitters under a solid immersion lens, New J. Phys. **24**, 103027 (2022).

[8] N.-J. Guo, S. Li, W. Liu, Y.-Z. Yang, X.-D. Zeng, S. Yu, Y. Meng, Z.-P. Li, Z.-A. Wang, L.-K. Xie, R.-C. Ge, J.-F. Wang, Q. Li, J.-S. Xu, Y.-T. Wang, J.-S. Tang, A. Gali, C.-F. Li, and G.-C. Guo, Coherent control of an ultrabright single spin in hexagonal boron nitride at room temperature, Nat. Commun. **14**, 2893 (2023).

[9] A. Sajid, M. J. Ford, and J. R. Reimers, Single-photon emitters in hexagonal boron nitride: A review of progress, Rep. Prog. Phys. **83**, 044501 (2020).

[10] I. Aharonovich, D. Englund, and M. Toth, Solid-state single-photon emitters, Nat. Photon. **10**, 631 (2016).

[11] A. Gottscholl, M. Kianinia, V. Soltamov, S. Orlinskii, G. Mamin, C. Bradac, C. Kasper, K. Krambrock, A. Sperlich, M. Toth, I. Aharonovich, and V. Dyakonov, Initialization and read-out of intrinsic spin defects in a van der Waals crystal at room temperature, Nat. Mater. **19**, 540 (2020).

[12] H. L. Stern, Q. Gu, J. Jarman, S. Eizagirre Barker, N. Mendelson, D. Chugh, S. Schott, H. H. Tan, H. Sirringhaus, I. Aharonovich, and M. Atatüre, Room-temperature optically detected magnetic resonance of single defects in hexagonal boron nitride, Nat. Commun. **13**, 618 (2022).

[13] J. Luo, Y. Geng, F. Rana, and G. D. Fuchs, Room temperature optically detected magnetic resonance of single spins in GaN, Nat. Mater. **23**, 512 (2024).

[14] T.-J. Lu, B. Lienhard, K.-Y. Jeong, H. Moon, A. Iranmanesh, G. Grosso, and D. Englund, Bright high-purity quantum emitters in aluminum nitride integrated photonics, ACS Photon. **7**, 2650 (2020).

[15] S. G. Bishop, J. P. Hadden, F. D. Alzahrani, R. Hekmati, D. L. Huffaker, W. W. Langbein, and A. J. Bennett, Room-Temperature quantum emitter in aluminum nitride, ACS Photon. **7**, 1636 (2020).

[16] X.-J. Wang, S. Zhao, H.-H. Fang, R. Xing, Y. Chai, X.-Z. Li, Y.-K. Zhou, Y. Zhang, G.-Y. Huang, C. Hu, and H.-B. Sun, Quantum emitters with narrow band and high Debye–Waller factor in aluminum nitride written by femtosecond laser, Nano Lett. **23**, 2743 (2023).

[17] J. B. Varley, A. Janotti, and C. G. Van de Walle, Defects in AlN as candidates for solid-state qubits, Phys. Rev. B **93**, 161201(R) (2016).

[18] Y. Xue, T. Wei, H. Chang, D. Liang, X. Dou, and B. Sun, Experimental optical properties of single-photon emitters in aluminum nitride films, J. Phys. Chem. C **125**, 11043 (2021).

[19] K. Y. Han, S. K. Kim, C. Eggeling, and S. W. Hell, Metastable dark states enable ground state depletion microscopy of nitrogen vacancy centers in diamond with diffraction-unlimited resolution, Nano Lett. **10**, 3199 (2010).

[20] K. Y. Han, D. Wildanger, E. Rittweger, J. Meijer, S. Pezzagna, S. W. Hell, and C. Eggeling, Dark state photophysics of nitrogen–vacancy centres in diamond, New J. Phys. **14**, 123002 (2012).

[21] M. Kianinia, C. Bradac, B. Sontheimer, F. Wang, T. T. Tran, M. Nguyen, S. Kim, Z.-Q. Xu, D. Jin, A. W. Schell, C. J. Lobo, I. Aharonovich, and M. Toth, All-optical control and super-resolution imaging of quantum emitters in layered materials, Nat. Commun. **9**, 874 (2018).

[22] See Supplemental Material at http://link.aps.org/supplemental/10.1103/PhysRevB.110.014109 for absorption and emission polarization plots for QE A and QE B, a single NV center in diamond PL characterization compared with the QE A and QE B, state population dynamics simulation of model III and model IV.

[23] H. L. Stern, C. M. Gilardoni, Q. Gu, S. Eizagirre Barker, O. F. J. Powell, X. Deng, S. A. Fraser, L. Follet, C. Li, A. J. Ramsay, H. H. Tan, I. Aharonovich, and M. Atatüre, A quantum coherent spin in hexagonal boron nitride at ambient conditions, Nat. Mater. (2024), doi:10.1038/s41563-024-01887-z.

[24] R. E. Fishman, R. N. Patel, D. A. Hopper, T.-Y. Huang, and L. C. Bassett, Photon-emission-correlation spectroscopy as an analytical tool for solid-state quantum defects, PRX Quantum **4**, 010202 (2023).

[25] R. N. Patel, D. A. Hopper, J. A. Gusdorff, M. E. Turiansky, T.-Y. Huang, R. E. K. Fishman, B. Porat, C. G. Van de Walle, and L. C. Bassett, Probing the optical dynamics of quantum emitters in hexagonal boron nitride, PRX Quantum **3**, 030331 (2022).

[26] M. Davanço, C. S. Hellberg, S. Ates, A. Badolato, and K. Srinivasan, Multiple time scale blinking in InAs quantum dot single-photon sources, Phys. Rev. B **89**, 161303(R) (2014).

[27] N. Chejanovsky, A. Mukherjee, J. Geng, Y. C. Chen, Y. Kim, A. Denisenko, A. Finkler, T. Taniguchi, K. Watanabe, D. B. R. Dasari, P. Auburger, A. Gali, J. H. Smet, and J. Wrachtrup, Single-spin resonance in a van der Waals embedded paramagnetic defect, Nat. Mater. **20**, 1079 (2021).

[28] A. L. Efros and D. J. Nesbitt, Origin and control of blinking in quantum dots, Nat. Nanotechnol. **11**, 661 (2016).

[29] P. Frantsuzov, M. Kuno, B. Jankó, and R. A. Marcus, Universal emission intermittency in quantum dots, nanorods and nanowires, Nat. Phys. **4**, 519 (2008).

[30] L. Robledo, H. Bernien, T. v. d. Sar, and R. Hanson, Spin dynamics in the optical cycle of single nitrogen-vacancy centres in diamond, New J. Phys. **13**, 025013 (2011).

[31] P. Khatri, A. J. Ramsay, R. N. E. Malein, H. M. H. Chong, and I. J. Luxmoore, Optical gating of photoluminescence from color centers in hexagonal boron nitride, Nano Lett. **20**, 4256 (2020).

[32] L. Hacquebard and L. Childress, Charge-state dynamics during excitation and depletion of the nitrogen-vacancy center in diamond, Phys. Rev. A **97**, 063408 (2018).

[33] D. Wirtitsch, G. Wachter, S. Reisenbauer, M. Gulka, V. Ivády, F. Jelezko, A. Gali, M. Nesladek, and M. Trupke, Exploiting ionization dynamics in the nitrogen vacancy center for rapid, high-contrast spin, and charge state initialization, Phys. Rev. Res. **5**, 013014 (2023).

[34] http://doi.org/10.17035/d.2024.0325944629.

[35] M. Berthel, O. Mollet, G. Dantelle, T. Gacoin, S. Huant, and A. Drezet, Photophysics of single nitrogen-vacancy centers in diamond nanocrystals, Phys. Rev. B **91**, 035308 (2015).